Chapter 4

Magnetic proximity induced Valley contrasting Quantum anomalous Hall Effect in Gr-$CrBr_3$ van der Waals heterostructure

4.1 Introduction

MPE [1] is an imperative tool in 2D vdW crystals, which exploit astonishing opportunities in modulating the electronic and nontrivial topological effects of neighboring material. Magnetic ordering via MPE and spin-orbit coupling (SOC) breaks time reversal symmetry (TRS) and opens a nontrivial global band gap near Dirac states, which induces nontrivial topological phases elucidated by the Chern number at zero external magnetic field [2, 3]. The quantum anomalous hall effect (QAHE) is one of such fascinating physical phenomena [4-6], creating dissipationless chiral nature of edge transport phenomena and manifest Hall conductance $\sigma_{xy}=e^2/h$ holding potential platform for low-power spintronic devices [7, 8]. Moreover, breaking of inversion symmetry in 2D honeycomb lattice has unequal carriers and binary degrees of freedom peaked at valleys K' and K, resulting in valley contrasting QAH effect [9]. The nonzero values of valleys are well preserved in Brillouin zone with no interaction among the valleys. Because of presence of localized valley, the Hall conductivity becomes nonzero, resulting in quantum valley Hall (QVH) effect [10, 11]. The valley contrasting QAHE has been theoretically predicted through external addition of bilayer non-magnetic system, superlattices, vacancies or antiferromagnetic (AFM) substrates on non-magnetic system having limitation in maintaining magnetic ordering [4, 12-15]. The coexistence of a long-range

M Bora, S K Behera, P Samal and P Deb, *Magnetic proximity induced valley-contrasting quantum anomalous Hall effect in a graphene-$CrBr_3$ van der Waals heterostructure*. Phys. Rev. B., 105:235422, 2022.

magnetic order along with relativistic effect [16] is the most crucial and challenging tasks to experimentally realize anomalous behaviour. In this regard, MPE depicts an effective approach to overcome the limitation by coupling long-range magnetic order induced by ferromagnetic (FM) or AFM vdW crystal along with SOC for realizing valley contrasting QAH effect [17]. Therefore, designing of robust valley localized QAH vdW crystal is of significant interest in nurturing further progress in this area.

Graphene is an appropriate model system for predicting topologically nontrivial phases because of its unique honeycomb lattice exhibiting high electron densities and long spin-relaxation length [18]. The pristine graphene is nonmagnetic in nature and has very weak intrinsic SOC of about 12 μeV with a very minute nontrivial band gap [19]. The coexistence of ferromagnetism and SOC in a material predicts valley contrasting QAHE [20]. Moreover, long-range magnetic ordering in topological insulator (TI) can be induced due to proximity coupling with ferromagnetic insulator (FI) [21, 22]. Recently, 2D magnetism has gained significant attention due to its intrinsic long-range magnetic order in atomically layered crystals [23] for realizing anomalous and topologically nontrivial state. In addition to SOC and magnetism, possible tuning of band gap by applying perpendicular electric field can extend an additional projection to engineer nontrivial topological phases [24, 25]. Therefore, such external perturbations can harness both SOC and magnetism by configuring the wave function localization induced exchange splitting in the electronic structure. This entails new opportunities by introducing 2D magnets with graphene coupled via proximity effect, SOC and external electric field in view of designing vdW heterostructure to generate quantum valley Hall (QVH) effect. In the current chapter, proximity coupled valley contrasting QAH effect is predicted in Gr-$CrBr_3$ vdW heterostructure with implication of relativistic effect, from *ab initio* density functional theory (DFT) simulation. and Wannier90 tools. The introduction of magnetic exchange and spin orbit interaction together enables to realize topological phases, with a particular emphasis on interface can be

envisioned towards dissipationless electronics. These computational findings will make the experimental fabrication highly favorable for developing valley contrasting QAH device prototype.

4.2 Model and Computational details

The ground state energy and electronic structure calculations are performed within the framework of *ab initio* DFT calculation by employing QE [26] software package, which uses the plane wave basis sets for computation. The PBE-GGA is employed to describe exchange and correlation functional [27]. To describe Cr-3d electrons, GGA+U method is considered [28] and the values of on-site Coulomb interaction U and exchange interaction J are set to be 3.0 and 0.9 eV, respectively. The plane wave cut of energy is set to 500 eV and a vacuum space of 22Å is used to avoid interactions between two adjacent layers. The 6 x 6 x 1 and 27 x 27 x1 Monkhorst-Pack grids are adopted for Gr-$CrBr_3$ heterostructure, respectively, to conduct first Brillouin zone integration. For vdW heterostructures, more accurate and expensive hybrid functional HSE06 [29] is adopted to achieve the optimized geometry structures and electronic state calculations including local potential distribution as implemented in the Vienna *ab initio* simulation package (VASP) [30]. The vdW correction with Grimme (DFT-D2) method [31] is considered in heterostructure calculation. For calculations of topological properties, maximally localized Wannier functions (MLWFs), Berry curvatures, anomalous Hall conductivity are constructed by employing the WANNIER90 package [32]. Wannier-Tool [33] is used for calculating the evolution of Wannier charge center (WCC). The Berry curvature is associated with Berry connection. Let us consider the wavefunction $|\Psi(R)\rangle$ for the m^{th} eigenstate of the Hamiltonian H(R), where R is parameterized with R = (R1, R2,……,Rm). The two overlapping wavefunctions, microscopically differentiated by ΔR in the parameter space R, can be written as [34]

$$\langle \Psi(R)|\Psi(R+\Delta R)\rangle = 1 + \Delta R\langle \Psi(R)|\boldsymbol{\nabla}_R\Psi(R)\rangle = e^{-i\Delta R A_m(R)} \quad (4.1)$$

where $A_m(R) = i\langle\Psi(R)|\boldsymbol{\nabla}_R|\Psi(R)\rangle$ is denoted as the Berry connection. It contemplates as a vector potential and the curl$\Omega_m(R) = \boldsymbol{\nabla}_R \times A_m(R)$, named as Berry curvature, which acts like a magnetic field in the parameter space R. By using gauge transformation between the Bloch electrons and real space Wannier functions, the Berry curvature is evaluated as [35]

$$\Omega(k) = \sum_m f_m \Omega_m(k), \tag{4.2}$$

$$\Omega_m(k) = -2Im \sum_{n\neq m} \frac{\langle\Psi_{mk}|v_x|\Psi_{nk}\rangle\langle\Psi_{nk}|v_y|\Psi_{mk}\rangle}{(E_n - E_m)^2} \tag{4.3}$$

where, the summation is over all occupied states in the momentum space, E_m is the eigenvalue of the Bloch electron wavefunctions $|\Psi_{mk}>$, f_m denotes the Fermi-Dirac distribution function, v_x and v_y are the velocity operators. Moreover, Chern number can be calculated by integrating the Berry curvature over the first Brillouin zone. Another alternative way to calculate the Chern topological invariant is by evaluating WCC. The correlation of Wannier functions to topology is linked by the matrix elements of the position operator in the Wannier basis to the Berry connection. The formulation of charge center as well as the spread can be written in terms of Bloch wavefunctions $|\Psi_{mk}>$ [36]

$$\overline{\boldsymbol{r}_n} = i\,\frac{V}{(2\pi)^3}\int d^3k \langle\Psi_{mk}|\boldsymbol{\nabla}_k|\Psi_{mk}\rangle \tag{4.4}$$

Since, the wavefunction of Bloch electron is associated with the Wannier functions having a gauge freedom.

The idea of using WCC for evaluating as a topological invariant, the expression of charge centers eq. (4.4) is proportional to Berry curvature. The topological invariant can be determined by calculating the WCC in 2D *k*-plane for occupied bands. The projection operator for occupied bands can be written as

$$\widehat{P_{k_y}} = \sum_{m\in O, k_x} |\Psi_{mk}><\Psi_{mk}| \tag{4.5}$$

where o in the summation denotes the occupied bands.

The eigenvalue should be considered for projected position operator defined as

$$\widehat{X_p}(k_y) = \widehat{P_{k_y}}\hat{X}\widehat{P_{k_y}} = C_v \quad (4.6)$$

where C_v corresponds to the valley Chern number, describing the topological invariance in the system.

For 2D system, we need to consider *k* and *t* as two independent coordinates, the Berry curvature will be the difference between the derivation with respect to *t* keeping k constant and derivation with respect to *k* keeping *t* constant. The integration of the Berry curvature over full period, difference in the projection operator will provide the total Chern number of a 2D system.

By obtaining the Chern number from the evolution of WCC and Berry curvature, the anomalous Hall conductivity can be evaluated by $\sigma_{xy} = \frac{e^2}{h} C_v$. The valley Chern number provides the information about the number of dissipationless transport channel present in the Gr-$CrBr_3$ vdW heterostructure.

4.3 Result and Discussions

4.3.1 Ground state crystal geometry

The stable crystal geometries with different views having interplanar spacing of 0.13 Å between graphene and monolayer $CrBr_3$ as shown in Figure 4.1 (a-c). at an interplanar spacing of 0.13 Å between two monolayers will hybridize effectively to induce proximity coupling along with SOC. The Gr-$CrBr_3$ vdW heterostructure system has obtained ground state energy configuration when ferromagnetic ordering and relativistic effect is considered for robust theoretical calculation. The dispersion correction is considered for optimization of interplanar spacing for close proximity interaction between graphene and $CrBr_3$. The interplanar spacing is contemplated as a vdW type. Figure 4.1 (b) displays the unit cell with two Cr atoms, where one situates at void site named as A and other one situates at top site named as B. Since, both A and B belong to

disparate sublattices of graphene, such heterointerfaces help in inducing staggered sublattice potential, which commend valley contrasting Hall effect in graphene [37] and designate to QVH phases.

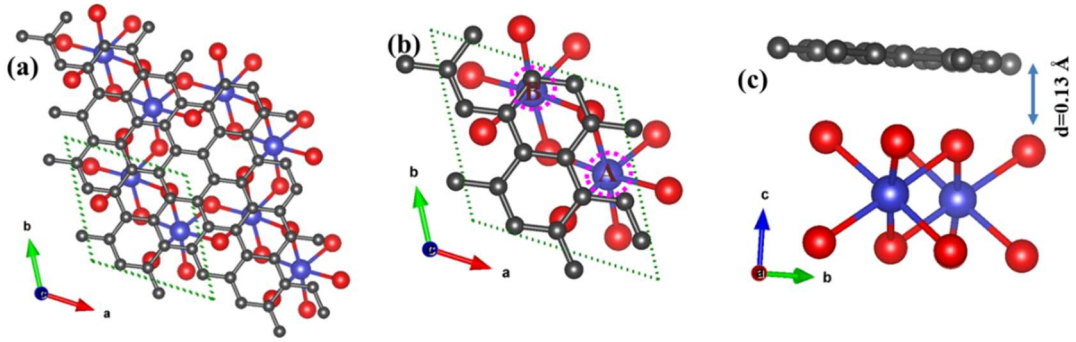

Figure 4.1: (a) Crystal geometry of Gr-$CrBr_3$ vdW heterolayer showing the top view of 2x2x1 supercell. (b) Top-view of the crystal structure of Gr-$CrBr_3$ heterostructure in unit cell. (c) Side view of the Gr-$CrBr_3$ unit cell with interplanar spacing notation of d=0.13 Å. The grey, blue and red balls describe carbon (C), chromium (Cr) and bromine (Br) respectively.

4.3.2 Electronic Structure

With the implications of relativistic effect, the electronic band structure of Gr-$CrBr_3$ heterostructure is plotted as shown in Figure 4.2 (a). A large global band gap of 178 meV is opened near Fermi level. The zoomed image of electronic band structure at M-K-Γ, band folding is seen near Fermi level, which utters signature of topology in heterostructure system. The band folding like a W shape at Fermi level is observed due to presence of SOC, staggered sublattice potential and proximity interaction in heterolayer system. The gapped state is mainly responsible due to SOC leading to splitting of energy levels having different orbitals and hybridization occurs among the orbitals due to proximity interaction as shown in Figure 4.2 (b) and (d). The TRS breaking is due to strong hybridization when graphene is coupled in close proximity with magnetic $CrBr_3$ and inversion symmetry is broken due to presence of uneven surface charge distribution in heterostructure system. In this regard, the consideration of SOC is important for splitting of energy level along with the opening of

global band gap by lifting the degeneracy, which speculates the possibility of valley contrasting anomalous behaviour as shown in zoomed image of Figure 4.2 (b). When graphene is located above $CrBr_3$, it becomes magnetically active due to proximity coupling between C p-orbitals and Cr d-orbitals, which relatively makes heterostructure magnetic in nature. As shown in Figure 4.2 (c), the heterostructure without consideration of SOC is a gapless system, which can be assigned to degeneracy of C spin-down p-orbitals at K point. The system is spin-polarized and Dirac cone is topologically protected by C_1 symmetry of heterostructure system. The position of Dirac cone near Fermi region strongly depends on the interlayer separation of d = 0.13 Å. The cyan and blue colour denote spin down and spin up states manifests electronic character of both graphene and $CrBr_3$ due to presence of magnetic proximity coupling. The total orbital contribution of Gr-$CrBr_3$ heterostructure system is observed as shown in Figure 4.2 (d), where conduction band region is mainly dominated by Cr d-orbitals and C p-orbitals. The hybridization among C p-orbitals and Cr d-orbitals is clearly evident from the dynamic behaviour of atomic orbitals due to proximity effect between graphene and ferromagnetic, $CrBr_3$. It is obvious that Cr d-orbitals will have more intense peak because of presence of intrinsic magnetic character. Therefore, stemming graphene on ferromagnetic $CrBr_3$ exerts staggered potential at a distinct interplanar spacing giving rise to

hybridization, charge rearrangement and induce magnetism via proximity integration.

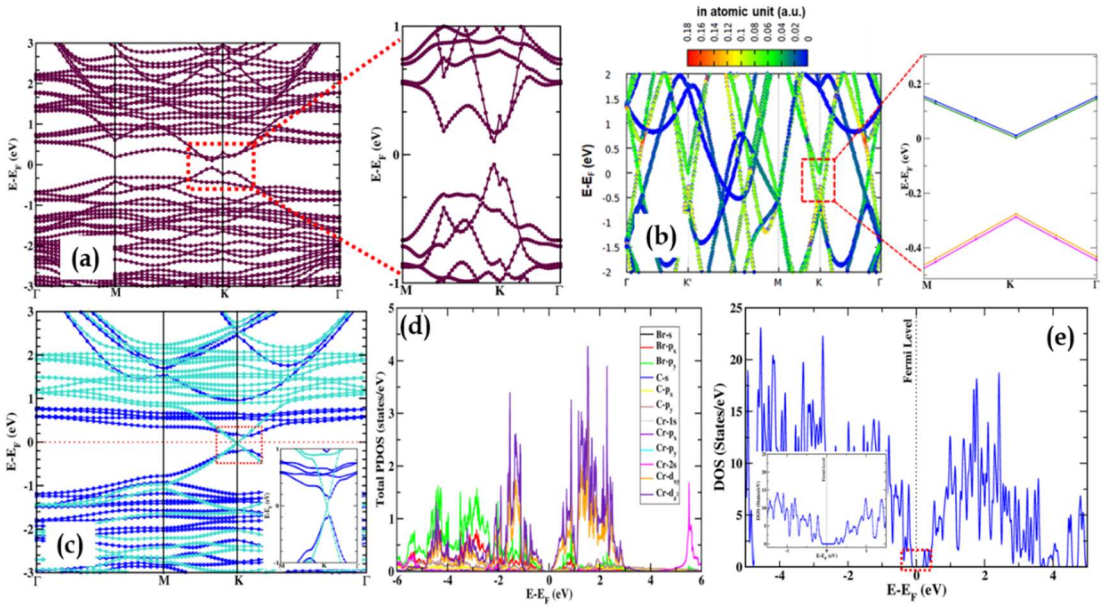

Figure 4.2: (a) Electronic band structure of Gr-$CrBr_3$ van der Waals heterostructure in presence of SOC. Zoomed-in picture shows band topology near Fermi level. (b) Projected band structure of Gr-$CrBr_3$ heterostructure with the implementation of relativistic effects. Zoomed image shows the splitting of energy level and gapped state at K-point. The colour bar represents the magnitude of projection (scale in atomic units). (c) Spin-polarized electronic band structure calculation of Gr-$CrBr_3$ heterostructure in absence of spin-orbit coupling (SOC). The blue and cyan line depicts spin-up and spin-down states, respectively. Inset shows the zoomed-in image of the Dirac cone near the Fermi level. (d) Projected density of states (PDoS) calculation of Gr-$CrBr_3$ heterostructure in presence of SOC. (e) Density of states (DOS) calculation for Gr-$CrBr_3$ heterostructure in presence of SOC. Zoomed-in inset shows the flat states near Fermi level.

The detailed projection of orbitals is displayed by plotting projected band of Gr-$CrBr_3$ heterostructure with inclusion of relativistic effect as shown in Figure 4.2(b). The direct band gap opening is observed near Fermi region at high symmetry points K and K′ owing to semiconducting nature of Gr-$CrBr_3$

heterostructure system supported with electronic band structure shown in Figure 4.2(a). Moreover, conduction band minimum (CBM) and valence band maximum (VBM) near Fermi energy at K point are mainly dominated by anti-bonding Br p_z orbitals, bonding between C p_y+p_z orbitals and Cr $d^2_{x-y}{}^2+d_{xy}$ orbitals denoted by blue, green and yellow colour, respectively. Due to presence of proximity coupling between graphene and $CrBr_3$, a strong hybridization occurs among C p-orbitals, Cr d-orbitals and splitting of these orbitals into different energy levels with inclusion of SOC. From overlapping states near Fermi level shown in Figure 4.2(c) to transition of gap opening in Figure 4.2(b) resembles hybridization *via* proximity effect between p_y+p_z orbitals of C atoms and $d^2_{x-y}{}^2+d_{xy}$ orbitals of Cr atoms. The opening of global band gap near K point corresponds to single topological phase transition. This topological phase transition occurs at valley K, which is mainly responsible for staggered AB sublattice potential exist due to close proximity integration. The zoomed image of Figure 4.2 (b) shows splitting of energy level and opening of global band gap at high symmetry point, which correlates well with Fig. 4.2 (a) implementing SOC effect.

Figure 4.2(e) shows density of states calculation for Gr-$CrBr_3$ heterolayer system. We observe flat states near Fermi level indicating opening of gap with implication of relativistic effect, which correlates well with band topology and PDoS of heterolayer system. The flat state near the Fermi level is also shown in the inset of Figure 4.2(e). The spike nature in DOS pattern speculates the presence of magnetic behaviour in hetero-bilayer system due to magnetic proximity coupling. Therefore, combined effect will trigger topological phases in Gr-$CrBr_3$ heterostructure system.

4.3.3 Electric field variation of Band topology and Local potential distribution

Along with relativistic effect and proximity coupling, vdW heterostructures also exhibit unique features on modulating electronic nature *via* externally

applying electric field in Gr-$CrBr_3$ heterostructure. We explore the variation of applied electric field in reverse (-Z-direction) and forward (+Z-direction) from -0.5 to 0.5 V/Å in Gr-$CrBr_3$ heterostructure system is displayed and is displayed in Figure 4.3 (a) and (b). It depicts the opening (179 to 183 meV) and closing of global band gap (177 to 173 meV) at high symmetry point near Fermi region (E_F). The band gap reduces i.e., tending to close with decreasing strength of electric field towards reverse (negative) bias as shown in Figure 4.3 (c). The modulating trend of band gap is found to be linear with the increasing strength of electric field. This indicates combination of electric field and SOC to be a convincing strategy to modulate electronic behaviour of Gr-$CrBr_3$ heterostructure. The band gap of hetero-bilayer system is found to be open as sufficient electric field is applied as shown in Figure 4.3 (b). When the strength of electric field is increased to 0.5 V/Å, band gap reaches around 183 meV, which is higher than that of 0 V/Å. When forward bias is applied in Z-direction of the heterostructure, redistribution of charge will leverage Rashba SOC extrinsically in Gr-$CrBr_3$ heterolayer and it has the possibility of breaking inversion symmetry.

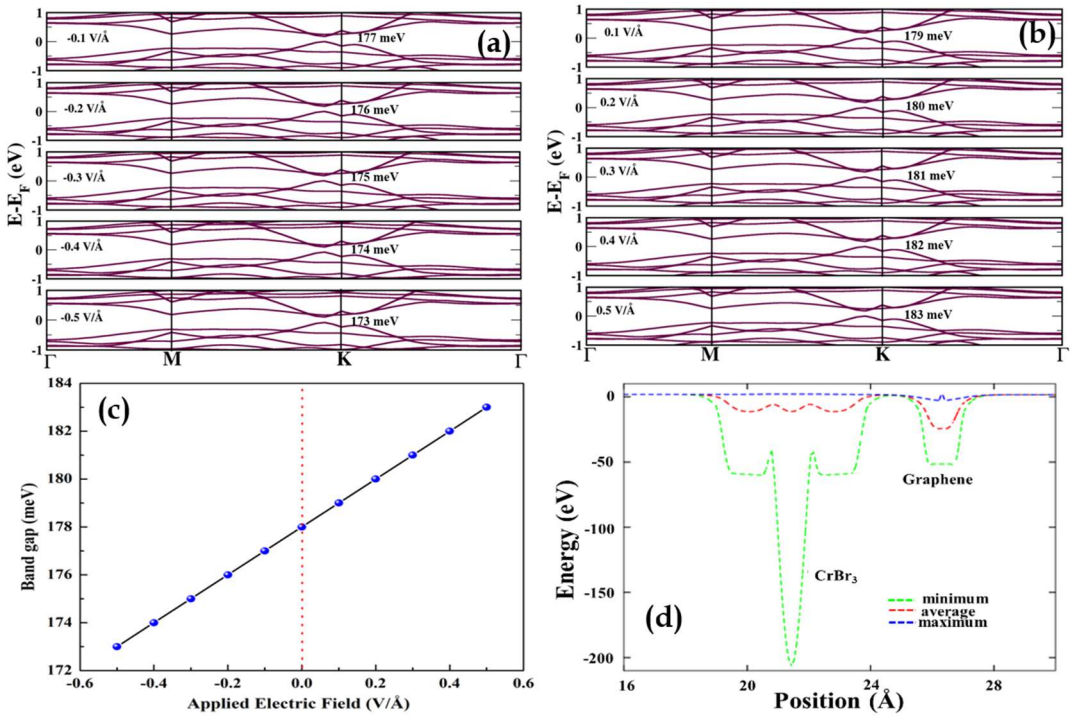

Figure 4.3: (a) Modulation of electronic band structure with the application of

perpendicular electric field in negative Z-direction from -0.1 to -0.5 V/Å in Gr-$CrBr_3$ bilayer system. (b) Modulation of band topology with the application of perpendicular electric field in positive Z-direction from 0.1 to 0.5 V/Å in Gr-$CrBr_3$ bilayer system. (c) Modulation of band gap with respect to external applied electric field effect in the heterostructure. (d) DFT simulated local potential distribution of the Gr-$CrBr_3$ heterostructure with contribution from both $CrBr_3$ monolayer and graphene sheet along Z-direction.

The inversion symmetry breaking can be realized using local potential distribution at both layers as described in Figure 4.3(d). The uneven distribution of electronic states over heterointerface gives rise to nonzero surface charge and subsequent electrostatic potential due to accumulation of local potential energy (shown in Figure 4.3(d)). The evenly distributed delocalization is clearly evident from local potential energy profile. The charge neutrality is noticed at interface due to presence of proximity interaction. This evenly distribution confirms average energy values at zero level with respect to various locations over the interface, indicating complete charge neutrality and inversion symmetry breaking. These combined analyses of band gap modulation and local potential energy profile shows delocalization of electronic states over the proximitized heterointerface.

4.3.4 Topological properties

To identify topologically nontrivial phase, we have calculated Berry curvatures and evolution of WCC for Gr-$CrBr_3$ heterostructure. We evaluate Berry curvature by integrating over K or K' symmetry point and can acquire Chern number for each valley from tight-binding Hamiltonian. It is seen from Figure 4.1 (b), each valleys take similar topological charge C_K=-$C_{K'}$=1 due to staggered AB sublattice potential. As the topological charge for valleys are similar, the total Chern number is vanishing C_K+$C_{K'}$=0. By subtracting the Chern number values for each valley K and K' contributes to QVH phase with C_v=(C_K-$C_{K'}$)/2=1. Since, the global band gap near K point does not close even in

absence of electric field, final value of valley Chern number remains invariant as C_v =1. Therefore, such behaviour is considered to have QAH phase exhibiting valley contrasting effect. Figure 4.4 (a) shows calculated Berry curvature Ω(k) summed over all occupied along high symmetry points in first Brillouin zone shown in Eqn (4.3). The inset in Figure 4.4 (a) shows Berry curvature distribution over 2D K-plane, where Fermi level has already been shifted into heterostructure band gap region. It is seen that Berry curvature is sizeable and takes opposite signs in vicinity of K and K' valleys revealing valley contrasting characteristic. The Berry curvatures are primarily localized near high symmetry points K and K'. The density of Berry curvature at valley K is slightly different from valley K', resulting in the inequality of Chern number obtained by valley K and K'. The Berry curvature is invariant under spatial inversion, which transforms K and K' into each other. Therefore, breaking of inversion and time reversal symmetry is the prime factor for realizing valley contrasting behaviour. The non-vanishing valley Chern number indicates opening of band gap to be topologically nontrivial, signifying the presence of QVH effect in heterostructure system. The nontrivial global band gap is found to be 178 meV, much larger than that of the reported QAH systems [5, 38]. This amplified SOC in graphene arises due to proximity coupling with ferromagnetic $CrBr_3$, breaking inversion symmetry of graphene plane and leads to strong Rashba SOC.

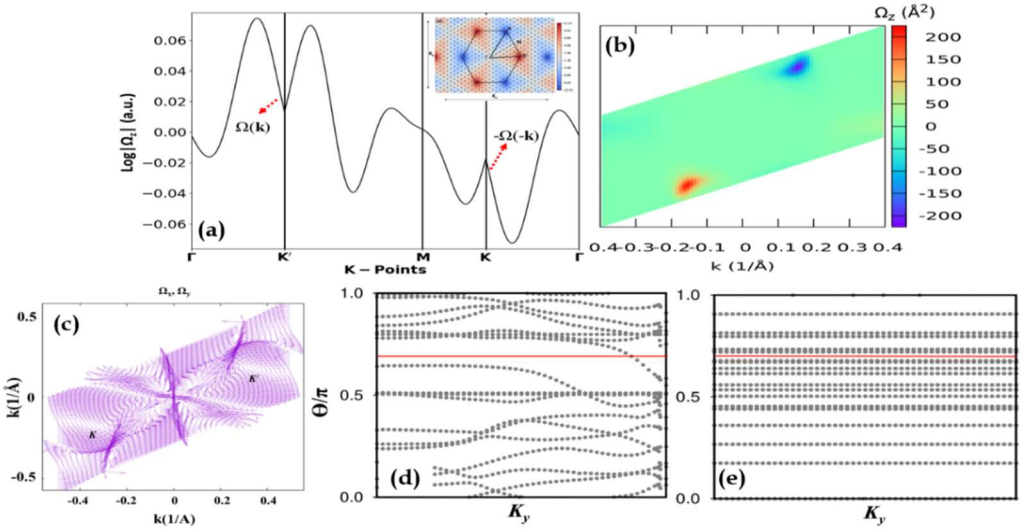

Figure 4.4: (a) Calculated Berry curvature of Gr-$CrBr_3$ heterostructure along high symmetry points. The red dashed arrow shows Ω(k) and -Ω(-k) (in logarithmic scale). The inset shows Berry curvature in 2D k-plane. (b) Density plots of Berry curvature for the occupied band for the first Brillouin zone of Gr-$CrBr_3$ heterostructure. (c) Spin configuration in the momentum space around K and K' for Gr-$CrBr_3$ bilayer system. (d) Evolution of Wannier charge center (WCC) for Gr-$CrBr_3$ bilayer system in the presence of SOC (e) in absence of SOC. The red solid line is reference line. Odd number times the reference line is crossed by evolution line indicating the system to be topologically nontrivial.

Figure 4.4 (b) describes density plots of Berry curvature for Gr-$CrBr_3$ heterostructure system. The Brillouin zone is parameterized over momentum space of heterostructure system. The Berry curvature exhibit both positive and negative values at valleys K and K' corroborating with Figure 4.4 (a) for realizing valley contrasting phenomena. It is clearly evident from Figure 4.4 (a), the valley is inverted and peaked at valley K' and K, respectively. The inverted and peaked valley can be correlated with blue and red colour in density plot of Berry curvature (as shown in Figure 4.4 (b)). The blue colour depicting Berry curvature around K' valley is divergent and red colour depicts K valley to be convergent, which primarily acts like a source and sink of Berry curvature. This is also quite evident from spin configuration plot as shown in Figure 4.4 (c), by normalizing the Berry curvature around K_x-K_y plane, we see the spin texture at K' and K to be divergent and convergent acting like a source and sink. The spin texture at K' and K are opposite to each other, correlating well with Figure 4.4 (a) and (b). This observation gives a clear insight of valley contrasting QAH phenomena. In this regard, Berry curvature will give rise to an anomalous transverse velocity for Bloch electrons under an in-plane longitudinal electric field [39]. Thus, charge carriers in K and K0 valley transmits in opposite direction realizing valley contrasting nature and giving rise to QVH effect. Figure 4.4 (d) displays evolution of WCC with respect to momentum space in Gr-$CrBr_3$ bilayer system as described in Eqn (4.6). The evolution of WCC in

momentum space is calculated by considering U(2N) non-Abelian Berry connection [40]. To show topological property via evolution of WCC, we implemented tight-binding model [41] for better visualization of topologically nontrivial states. It is clearly evident that only once the evolution line crosses red solid reference line with implementation of relativistic effect in heterostructure system, indicating the system to be topologically nontrivial. No crossing of evolution line through reference line is observed leading to topologically trivial state in absence of SOC as shown in Figure 4.4 (e). Therefore, odd winding number of WCC clearly signify valley contrasting phenomena and topologically nontrivial state in Gr-$CrBr_3$ vdW heterostructure.

4.3.4 Anomalous Hall behaviour

Figure 4.5 (a) illustrates Hall coefficient in Gr-$CrBr_3$ heterostructure as a function of chemical potential at different temperature. Gr-$CrBr_3$ heterostructure system shows a shifting near Fermi level (E_F) towards positive chemical potential, which signifies active participation of p-type carrier concentration. Moreover, shifting of peak towards p-type carrier concentration attributes due to magnetic proximity coupling between graphene and ferromagnetic $CrBr_3$. There is a slight decrease in value of Hall coefficient in context of temperature differing from 100 K to 300 K, which can be neglected. As a consequence of valley contrasting nature obtained from Berry curvature, an anomalous Hall conductivity is observed in heterostructure system. The nature of anomalous Hall effect (AHE) is explained by Berry phase of Bloch electron, which is induced by relativistic implications in presence of magnetization due to proximity effect modelled by complex transfer integrals [42].

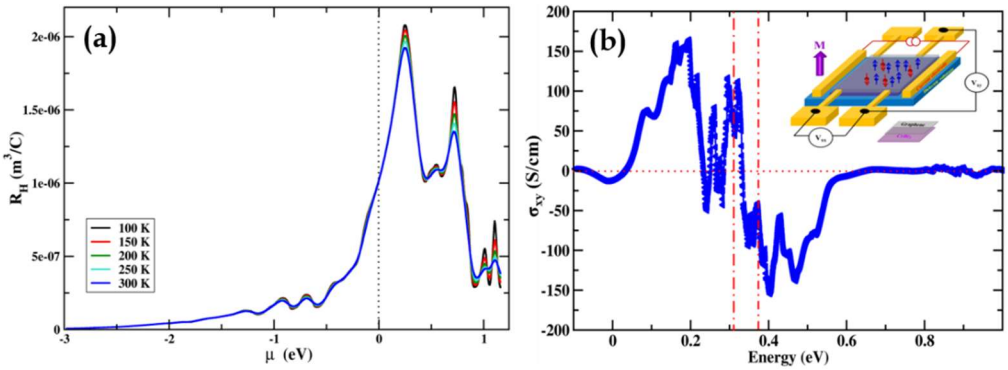

Figure 4.5: (a) Calculation of Hall coefficient in Gr-$CrBr_3$ heterostructure with respect to the chemical potential at different temperature. (b) The calculated anomalous Hall conductivity as a function of energy. The two dot-dashed lines depict the two valleys. Inset displays scheme of QVH effect in the vdW heterostructure of graphene on monolayer $CrBr_3$.

Figure 4.5 (b) shows calculated σ_{xy} with respect to energy. The extreme maxima of the valley K and K' is denoted by red dot-dashed line signifying presence of valley localized quantum Hall effect. The anomalous Hall conductivity (AHC) is obtained intrinsically in absence of external electric field because of nonzero surface charge and delocalized electrostatic potential created at heterointerface via magnetic proximity coupling. The plateau near zero energy in AHC hints us possibility of possessing quantization of Landau levels due to presence of binary degrees of freedom resulting valley contrasting QAH effect. However, small plateau near zero energy also signifies the existence of Hall conductivity in the limit of low concentration intrinsically due to magnetic proximity interaction. The inset in Figure 4.5 (b) depicts schematic model of a QVH device connected with a current electrode for applying the bias current in Gr-$CrBr_3$ heterostructure system for measuring Hall resistance. The presence of SOC and proximity coupling of ferromagnetic $CrBr_3$ with graphene leads in breaking of time reversal symmetry for realizing QVH effect. However, alongside proximity coupling and SOC, the QVH phase also occurs with application of bias current, which modifies the carrier density close to zero. Moreover, the domains of magnetic material strongly interact with applied bias current, which

electrically tunes polarization of magnetic domains [33]. The Hall resistance can also be driven by proximity coupling with ferromagnetic $CrBr_3$. We leverage this flexibility in our device prototype. Modelling of such device prototype can be introduced in any platform for experimental realization of QVH effect.

4.4 Concluding Remarks

In this chapter we systematically investigate magnetic proximity induced quantum valley Hall (QVH) effect in Gr-$CrBr_3$ heterostructure based on ab initio DFT simulations, Wannier90 package and WannierTool. The global band gap of 178 meV is opened near high symmetry point at Fermi region with implications of relativistic effect, which can be easily modulated with external electric field or incorporation of staggered AB sublattice potential. This intrinsically breaks inversion symmetry of graphene bipartite sublattice leading to strong Rashba SOC. In addition to SOC and magnetism, external electric field helps to modulate electronic properties of hetero-bilayer system. The calculated Berry curvature indicates that system can represent characteristics of valley contrasting QAH effect. The valley contrasting nature is also evident from nonzero value of two extreme valleys peaked at K' and K, typically behaved like a source and sink of Berry curvature. The odd winding number (valley Chern number C_v=1) associated from WCC clearly signifies breaking of time reversal symmetry, possessing topologically nontrivial state. The AHC is obtained in absence of external electric field due to nonzero surface charge and local potential originated at interface via magnetic proximity coupling. The calculated value of Hall coefficient in the heterostructure system is found to be shifted towards right (positive chemical potential) due to the magnetic proximity coupling between graphene and ferromagnetic $CrBr_3$. Therefore, Gr-$CrBr_3$ heterostructure system provide a promising platform to detect valley contrasting QAH Effect. This finding will engulf new approach in realizing experimental implications in unveiling possible vdW systems for QVH effect.

References

[1] Bora, M. and Deb, P. Magnetic Proximity effect in two-dimensional van der Waals heterostructure. *Journal of Physics: Materials*, 4:034014, 2021.

[2] Hasan, M. Z. and Kane, C. L. Colloquium: Topological insulators. *Review of Modern Physics*, 82:3045, 2010.

[3] Qi, X. -L., Hughes, T. L. and Zhang, S. -C. Topological field theory of time-reversal invariant insulators. *Physical Review B*, 78:195424, 2008.

[4] Fu, H., Liu, C. -X. and Yan, B. Exchange bias and quantum anomalous Hall effect in the MnBi2Te4/CrI3 heterostructure. *Science Advances*, 6:eaaz0948, 2020.

[5] Yu, R., Zhang, W., Zhang, H. J., Zhang, S. C., Dai, X. and Fang, Z. Quantized anomalous Hall effect in Magnetic topological insulators. *Science*, 329:61, 2010.

[6] Haldane, F. D. M. Model for a Quantum Hall effect without Landau levels: Condensed-matter realization of the "Parity Anomaly". *Physical Review Letters*, 61:2015, 1988.

[7] Chang, C. -Z., Zhao, W., Kim, D. Y., Zhang, H., Assaf, B. A., Heiman, D., Zhang, S. C., Liu, C., Chan, M. H. W. and Moodera, J. S. High-precision realization of robust quantum anomalous Hall state in a hard ferromagnetic topological insulator. *Nature Materials*, 14:473, 2015.

[8] Ou, Y., Liu, C., Jiang, G., Feng, Y., Zhao, D., Wu, W., Wang, X. -X., Li, W., Song, C., Wang, L. -L., Wang, W., Wu, W., Wang, Y., He, K., Ma, X. -C. and Xue, Q. -K. Enhancing the quantum anomalous Hall effect by magnetic cooping in a topological insulator. *Advanced Materials*, 30:1703062, 2018.

[9] Qiao, Z., Jiang, H., Li, X., Yao, Y. and Niu, Q. Microscopic theory of quantum anomalous Hall effect in graphene. *Physical Review B*, 85:115439, 2012.

[10] Lee, J., Mak, K. F. and Shan, J. Electrical control of the valley Hall effect in bilayer MoS2 transistors. *Nature Nanotechnology*, 11:421, 2016.

[11] Mak, K. F., Mcgill, K. L., Park, J. and Mceuen P. L. The valley Hall effect in MoS_2 transistors. *Science*, 344:1489, 2014.

[12] Zhai, X. and Blanter, Y. M. Spin-valley polarized quantum anomalous Hall effect and a valley-controlled half-metal in bilayer graphene. *Physical Review B*, 101:155425, 2020.

[13] Martiny, J. H. J., Kaasbjerg, K. and Jauho, A. -P. Tunable valley Hall effect in gate-defined graphene superlattices. *Physical Review B*, 100:155414, 2019.

[14] Xu, L., Yang, M., Shen, L., Zhou, J., Zhu, T. and Feng, Y. P. Large valley splitting in monolayer WS_2 by proximity coupling to an insulating antiferromagnetic substrate. *Physical Review B*, 97:041405(R), 2018.

[15] Olsen, T. and Souza, I. Valley Hall effect in disordered monolayer MoS_2 from first principles. Physical Review B, 92:125146, 2015.

[16] Island, J. O., Cui, X., Lewandowski, C., Khoo, J. Y., Spanton, E. M., Zhou, H., Rhodes, D., Hone, J. C., Taniguchi, T., Watanabe, K., Levitov, L. S., Zaletel, M. P. and Young, A. F. Spin-orbit driven band inversion in bilayer graphene by the van der Waals proximity effect. *Nature*, 571:85, 2019.

[17] Nagata, K., Matsushita, S. Y., Pan, X. -C., Huynh, K. -K. and Tanigaki, K. Large-proximity-induced anomalous Hall effect in $Bi_{2-x}Sb_xTe_{3-y}Se_y/Cr_2Ge_2Te_6$ heterostructure prepared by film transfer method. *Physical Review Materials*, 5:024208, 2021.

[18] Zutic, I., Fabian, J. and Sarma, S. Spintronics: Fundamentals and applications. *Review Modern Physics*, 76:323, 2004.

[19] Gmitra, M., Konschuh, S., Ertler, C., Ambrosch-Draxl, C. and Fabian, J. Band-structure topologies of graphene: Spin-orbit coupling effects from first principles. *Physical Review B*, 80:235431, 2009.

[20] Ding, J., Qiao, Z., Feng, W., Yao, Y. and Niu, Q. Engineering quantum anomalous/valley Hall states in graphene via metal-atom adsorption: An *ab-initio* study. *Physical Review B*, 84:195444, 2011.

[21] Hogl, P., Frank, T., Zollner, K., Kochan, D., Gmitra, M. and Fabian, J. Quantum Anomalous Hall Effects in Graphene from Proximity-Induced Uniform and Staggered Spin-Orbit and Exchange Coupling. *Physical Review Letter*, 124:136403, 2020.

[22] Zhang, J., Zhao, B., Yao, Y. and Yang, Z. Robust quantum anomalous Hall effect in graphene-based van der Waals heterostructures. *Physical Review B*, 92:165418, 2015.

[23] Burch, K. S., Mandrus, D. and Park, J. -G. Magnetism in two-dimensional van der Waals materials. *Nature*, 563:47, 2018.

[24] Alsharari, A. M., Asmar, M. M. and Ulloa, S. E. Proximity-induced topological phases in bilayer graphene. *Physical Review B*, 97:241104(R), 2018.

[25] McCann, E. Asymmetry gap in the electronic band structure of bilayer graphene. *Physical Review B*, 74:161403(R), 2006.

[26] Giannozzi, P., Baroni, S., Bonini, N., Calandra, M., Car, R., Cavazzoni, C., Ceresoli, D., Chiarotti, G. L., Cococcioni, M., Dabo, I., Corso, A. D., de Gironcoli, S., Fabris, S., Fratesi, G., Gebauer, R., Gerstmann, U., Gougoussis, C., Kokalj, A., Lazzeri, M., Martin-Samos, L., Marzari, N., Mauri, F., Mazzarello, R., Paolini, S., Pasquarello, A., Paulatto, L., Sbraccia, C., Scandolo, S., Sclauzero, G., Seitsonen, A. P., Smogunov, A., Umari, P., and Wentzcovitch, R. M. QUANTUM ESPRESSO: a modular and open-source software project for quantum simulations of materials. *Journal of Physics: Condensed Matter*, 21(39):395502, 2009.

[27] Perdew, J. P., Burke, K. and Ernzerhof, M. Generalized gradient approximation made simple. *Physical Review Letter*, 77:3865, 1996.

[28] Liechtenstein, A. I., Anisimov, V. I. and Zaanen, J. Density-functional theory and strong interactions: Orbital ordering in Mott-Hubbard insulators *Physical Review B*, 52:R5467, 1995.

[29] Heyd, J. and Scuseria, G. E. Hybrid functionals based on a screened Coulomb potential. *Journal of Chemical Physics*, 118:8207, 2003.

[30] Kresse, G. and Furthmuller, J. Efficient iterative schemes for *ab initio* total-energy calculations using a plane-wave basis set. *Physical Review B*, 54:11169, 1996.

[31] Grimme, S. Semiempirical GGA-type density functional constructed with a long-range dispersion correction. *Journal of Computational Chemistry*, 27:1787, 2006.

[32] Marzari, N., Mostofi, A. A., Yates, J. R., Souza, I. and Vanderbilt, D. Maximally localized Wannier functions: Theory and applications. *Review Modern Physics*, 84:1419, 2012.

[33] Wu, Q., Zhang, S., Song, H. -F., Troyer, M. and Soluyanov, A. A. WannierTools: An open-source software package for novel topological materials. *Computer Physics Communications*, 224:405, 2018.

[34] Weng, H., Rui, Y., Xiao, H., Xi, D. and Zhong, F. Quantum anomalous Hall effect and related topological electronic states. *Advances in Physics*, 64:227, 2015.

[35] Wang, X., Yates, J. R., Souza, I. and Vanderbilt, D. *Ab initio* calculation of the anomalous Hall conductivity by Wannier interpolation. *Physical Review B*, 74:195118, 2006.

[36] Marzari, N. and Vanderbilt, D. Maximally localized generalized Wannier functions for composite energy bands. *Physical Review B*, 56:12847, 1997.

[37] Giovannetti, G., Khomyakov, P. A., Brocks, G., Kelly, P. J. and van den Brink, J. Substrate-induced band gap in graphene on hexagonal boron

nitride: *Ab initio* density functional calculations. *Physical Review B*, 76:073103, 2007.

[38] Wang, Q. -Z., Liu, X., Zhang, H. -J., Samarth, N., Zhang, S. -C. and Liu, C. -X. Quantum Anomalous Hall Effect in Magnetically Doped InAs/GaSb Quantum Wells. *Physical Review Letter*, 113:147201, 2014.

[39] Xiao, D., Chang, M. -C. and Niu, Q. Berry phase effects on electronic properties. *Review Modern Physics*, 82:1959, 2010.

[40] Soluyanov, A. A. and Vanderbilt, D. Computing topological invariants without inversion symmetry. *Physical Review B*, 83:235401, 2011.

[41] Schulz, S. and Czycholl, G. Tight-binding model for semiconductor nanostructures. *Physical Review B*, 72:165317, 2005.

[42] Onoda, M. and Nagaosa, N. Topological Nature of Anomalous Hall Effect in Ferromagnets. *Journal of the Physical Society of Japan*, 71:19, 2002.